Electronic Supplementary Material (ESI) for ChemComm.

Electronic Supplementary Information (ESI)

Graphene oxide as a structure-directing agent for the two-dimensional interface engineering of sandwich-like graphene/g-C_3N_4 hybrid nanostructures with enhanced visible-light photoreduction of CO_2 to methane

Wee-Jun Ong, Lling-Lling Tan, Siang-Piao Chai* and Siek-Ting Yong

Multidisciplinary Platform of Advanced Engineering, Chemical Engineering Discipline, School of Engineering, Monash University, Jalan Lagoon Selatan, Bandar Sunway, 47500 Selangor, Malaysia.

* Corresponding author.

Tel: +603-5514 6234; Fax: +603-5514 6207

E-mail address: chai.siang.piao@monash.edu

(1) Detailed experimental procedures

Chemicals

Natural graphite powder (average particle size of 45 µm, > 99.99%), hydrogen peroxide (H_2O_2, 30%), potassium manganese oxide ($KMnO_4$, ≥ 99.0%), phosphorus pentoxide (P_2O_5, ≥ 98.0%), potassium persulfate ($K_2S_2O_8$, ≥ 99.0%), urea (≥ 99.0%), thiourea (≥ 99.0%), melamine (99%), dicyandiamide (99%), terephthalic acid (TA, 98%) and sodium hydroxide (NaOH, 98%) were supplied by Sigma Aldrich. In addition, sulphuric acid (H_2SO_4, 95%–97%), hydrochloric acid (HCl, 70%) and ethanol (96%) were purchased from Chemolab. All reagents were of analytical grade and used without further purification. Deionized (DI) water (> 18.2 MΩ cm resistivity) was used in the whole experiment.

Preparation of graphene oxide

Graphite oxide (GO) was synthesized by modified Hummers' method through oxidation of graphite powder.[1,2] In detail, 3 g of graphite powder was added into an 80 °C mixture containing 12 mL of concentrated H_2SO_4, 2.5 g of P_2O_5 and 2.5 g of $K_2S_2O_8$. The mixture was stirred for 4.5 h at 80 °C. The mixture was then cooled to room temperature and diluted with 500 mL of DI water. Successively, the mixture was filtered and washed with DI water until the pH of the filtrate water became neutral. The product was then dried at 70 °C in an oven overnight. This pre-oxidized graphite was then dispersed into 120 mL of cold (0 °C) concentrated H_2SO_4. After that, 15 g of $KMnO_4$ was gradually added under stirring and the temperature of the mixture was kept below 20 °C by cooling. This resulted in the formation of a thick dark green paste. Successively, the mixture was stirred for 2 h at room temperature followed by diluting with 250 mL of DI water in an ice bath to keep the temperature below 50 °C. After another 2 h of stirring, the dark brownish solution was further diluted with 700 mL of DI water. Subsequently, 20 mL of H_2O_2 was slowly added into the mixture and a brilliant yellow product was formed along with bubbling. The mixture was then filtered and washed with 1 L of HCl to remove metal ions followed by 1 L of DI water to remove the acid. The filter cake was dispersed in water by mechanical agitation. Low speed centrifugation was performed at 1000 rpm for 2 min. The supernatant underwent high speed centrifugation steps at 10000 rpm for 30 min to remove small pieces of graphene oxide and water soluble by-products. Finally, the sediment was dried in air at 60 °C for 24 h. The GO product was ground into powder. To obtain graphene oxide sheets, a measured amount of GO was dispersed in deionized water and subjected to ultrasonication for 1 h at 40 kHz and 180 W using a table-top ultrasonic cleaner. The schematic diagram of the synthesis of graphene oxide sheets is shown in Fig. S1.

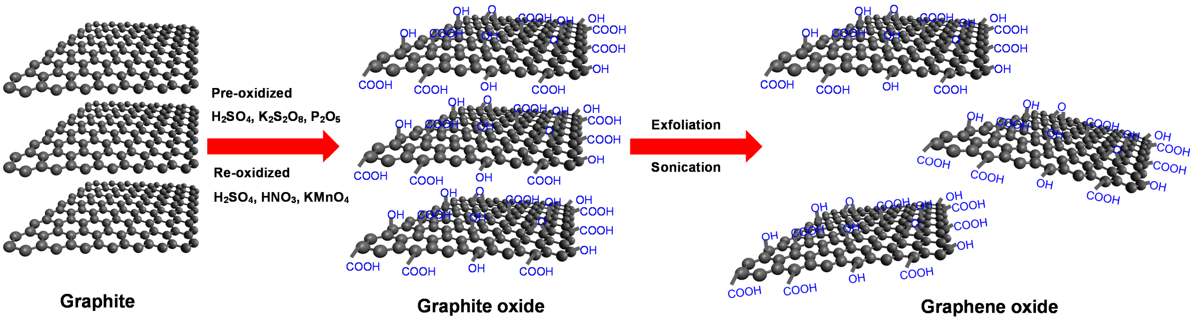

Fig. S1 Schematic illustration of the overall steps used in the preparation of graphene oxide sheets *via* modified Hummers' method.

Fabrication of graphene/g-C_3N_4 (GCN) hybrid nanocomposites

The GCN hybrid nanocomposites were fabricated *via* a facile one-pot impregnation-thermal reduction strategy. A typical synthesis route of GCN photocatalysts is depicted in Fig. 1 in the manuscript. In a typical synthesis, a measured amount of GO was dispersed in 100 mL of DI water and ultrasonicated for 1 h at ambient condition to fully exfoliate GO into graphene oxide sheets. Next, 6 g of urea was added and the mixture was vigorously stirred for 1 h at room temperature. Then the obtained solution was concentrated into a paste by heating at 100 ^{o}C under stirring for complete water evaporation. The resulting product was collected and dried in an oven at 70 ^{o}C for 12 h. The dried sample was grinded into powders and placed into a crucible with a cover to reduce the sublimation of urea during thermal polymerization. Finally, the GCN nanocomposite was produced by annealing at 520 ^{o}C for 2.5 h in a furnace with a ramping rate of 10 ^{o}C min^{-1} in order to thermally polymerize urea into g-C_3N_4 and reduce graphene oxide to graphene simultaneously. The resultant grey product was collected and ground in an agate mortar into powders. A series of GCN nanocomposites with different mass ratios of graphene to g-C_3N_4 was prepared by changing the amounts of GO (0.05 g, 0.10 g, 0.15 g and 0.20 g) and denoted as GCN-0.05, GCN-0.10, GCN-0.15 and GCN-0.20, respectively. Pure g-C_3N_4 (CN-Urea) was synthesized by directly heating urea in a semi-closed crucible with a cover at 520 ^{o}C for 4 h. For comparison with different nitrogen-containing precursors, thiourea, melamine and dicyandiamide were also used as the starting materials for the synthesis of g-C_3N_4 under the same preparation conditions. The obtained samples were denoted as CN-Thiourea, CN-Melamine and CN-Dicyandiamide, respectively. Similarly, the graphene-modified g-C_3N_4 photocatalysts with various nitrogen-containing precursors such as thiourea, melamine and dicyandiamide were fabricated to compare the efficiency of charge carriers recombination with GCN-Urea under similar graphene loading. The as-prepared samples were denoted as GCN-Thiourea, GCN-Melamine and GCN-Dicyandiamide, respectively.

Characterization techniques

The surface morphology of the samples was analyzed by field emission scanning electron microscopy (FESEM) and transmission electron microscopy (TEM). FESEM images were performed on Hitachi SU8010. High resolution TEM (HRTEM) images were taken with a JEOL JEM-2100F microscope operated at 200 kV. The energy loss spectroscopy (EELS) spectrum was obtained on a JEOL JEM-2800 microscope operated at 200 kV equipped with an EELS spectrometer. The TEM sample was created by depositing a drop of diluted suspensions in ethanol on a lacey-film-coated copper grid. Powder X-ray diffraction (XRD) patterns were obtained over the diffraction angle range (2θ) 5–90^o on a Bruker D8 Discover X-Ray Diffractometer using Ni-filtered Cu-Kα radiation (λ = 0.154056 nm) as the X-ray source at a scan rate of 0.02^o s^{-1} operated at 40 kV and 40 mA. The structural information for samples was measured by a Fourier transform spectrophotometer (FTIR, Thermo-Nicolet iS10) using a standard KBr pellet technique. Each spectrum was recorded as the average of 32 scans with a resolution of 4 cm^{-1} from 4000 to 400 cm^{-1}. Ultraviolet-visible (UV-Vis) absorbance spectra were determined using a UV-Vis spectrophotometer (Agilent, Cary 100) equipped with an integrated sphere. The absorbance spectra of the samples were analyzed at ambient temperature in the wavelength range of 200–800 nm. The X-ray photoelectron spectroscopy (XPS) was performed on a Kratos Axis-Ultra DLD instrument with a monochromatized Al Kα X-ray source (15 kV, 200 W) at a pressure of 7.6×10^{-9} Torr and a pass energy of 20 eV. All the binding energies were referenced to the C 1s peak at 284.6 eV of the surface carbon. Peak deconvolution and quantification of elements were accomplished using OriginPro 8.5. Thermogravimetric analysis (TGA) measurement was performed from the room temperature to 900 ^{o}C with a heating rate of 10 ^{o}C min^{-1} under N_2 atmosphere (TA

Instrument Q50). The photoluminescence (PL) emission spectra were measured on a fluorescence spectrometer (Perkin Elmer, LS55) at an excitation wavelength of 370 nm with the scanning speed of 600 nm min^{-1}. The widths of excitation slit and emission slit were both 10 nm. All the measurements were performed at room temperature. For the initial studies, the precursors-derived pure g-C_3N_4 and GCN-precursors were characterized using PL analysis. The details of the initial studies were discussed in Section 2 of the ESI.

Evaluation of photocatalytic reduction of CO_2

The photocatalytic reduction of CO_2 was conducted at ambient temperature and atmospheric pressure in a homemade, continuous gas flow reactor as reported in our previous work.[3-6] The experimental set-up is depicted in Fig. S2. Highly pure CO_2 (99.999%) was bubbled through water (sacrificial reagent) to produce a mixture of CO_2 and water vapor into the photoreactor. The flow rate of CO_2 was fixed at 5 mL min^{-1}. Prior to irradiation, CO_2 was purged through the quartz tube loaded with coated photocatalysts on glass rods for 30 min to remove any excess air and to ensure complete adsorption of gas molecules. The visible light source was then turned on to initiate the photocatalytic reaction. The reactant gas was in contact with the photocatalyst under the illumination of 15 W energy-saving daylight bulb (Philips, TORNADO 15 W WW E27 220–240 V 1CT) as the visible light source. The temperature in the reactor was closely monitored with a thermocouple attached to a digital temperature reader. The average intensity of the light was measured to be 8.5 mW cm^{-2} by utilizing a pyranometer (Kipp and Zonen type CMP 6). The distance apart between the light source and the photoreactor was fixed to be 5 cm. During the CO_2 photoreduction process, the product gases were collected at 1 h intervals and were analyzed by an Agilent 7890A gas chromatography (GC), equipped with a flame ionized detector (FID). The entire photoreaction system was enclosed in a black box to avoid any interference of light source from the surrounding. The photocatalytic experiments were performed in duplicate under similar reaction conditions to ensure the reproducibility of the catalytic activity in which consistent results with significant small variations were obtained. A series of control experiments was conducted to ensure that the CH_4 product formed was due to the photoreduction of CO_2 and not from the photodecomposition of organic residues on the catalyst surface. The total yield of CH_4 produced was calculated using eqn 1.

$$\text{Total CH}_4\text{ yield }\left(\mu\text{mol CH}_4\text{ g}_{\text{catalyst}}{}^{-1}\right) = \frac{\text{total amount of CH}_4\text{ produced }(\mu\text{mol})}{\text{mass of photocatalysts used }(\text{g}_{\text{catalyst}})} \qquad (1)$$

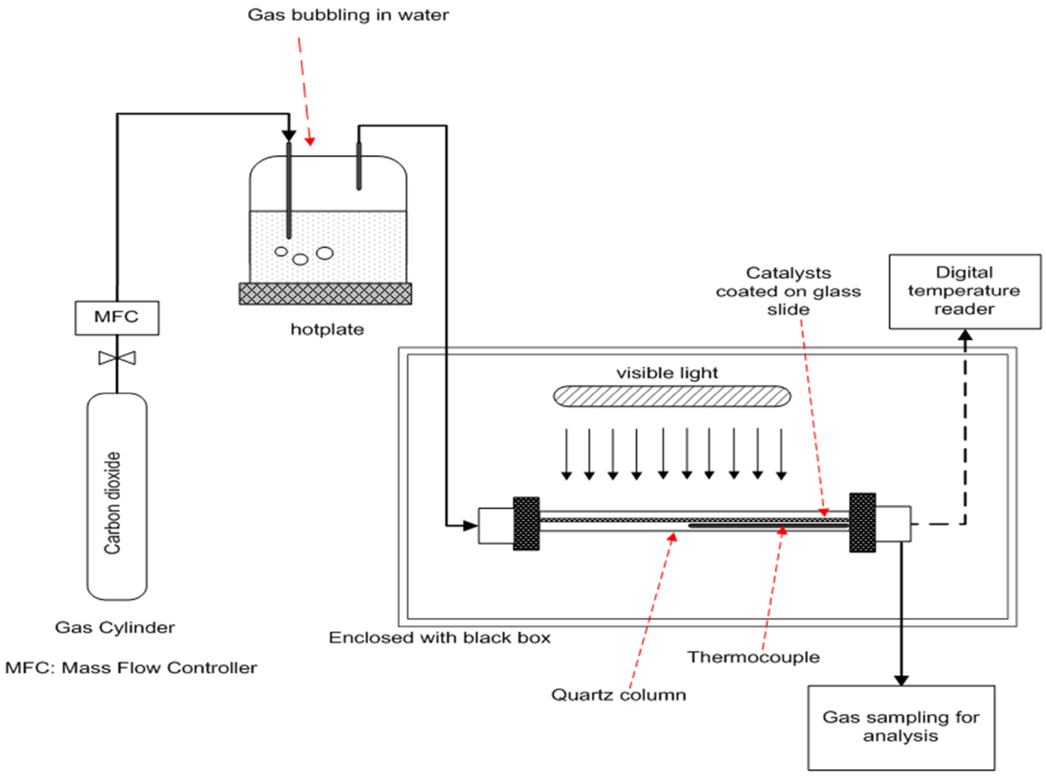

Fig. S2 Experimental set-up for the photocatalytic reduction of CO_2 under visible light irradiation.

Analysis of hydroxyl radicals (•OH)

The PL technique, which uses TA as a probe molecule, was employed to detect the formation of •OH radicals at the illuminated catalyst/water interface. TA readily reacts with •OH to generate a highly fluorescent product of 2-hydroxyterephthalic acid (TAOH), which can be detected at a PL signal of 425 nm.[7] The amount of •OH produced is proportional to the PL intensity. In brief, 30 mg of each sample (pure g-C_3N_4 and GCN) was suspended in 50 mL of solution containing 5 mM of TA with a concentration of 10 mM of NaOH. Prior to light irradiation, the suspension was stirred in the dark for 30 min. Upon light irradiation for 10 h of reaction, 3 mL of the reaction solution was obtained and centrifuged (13500 rpm, 30 min). Then the PL spectra of the produced TAOH were measured on a Perkin Elmer LS55 fluorescence spectrometer with an excitation wavelength of 315 nm and the emission spectra were scanned from 350 to 550 nm.

(2) PL analysis of other precursors-derived pure g-C_3N_4 and GCN-precursor systems

PL spectral analysis was employed to study the efficiency of charge carrier trapping and recombination in the pure g-C_3N_4 synthesized from different precursors (Fig. S3A) and graphene-modified g-C_3N_4 developed using graphene oxide and various nitrogen-containing precursors as the starting materials (Fig. S3B). As depicted in Fig. S3A, the PL peak emission intensity was found to follow the order: CN-Dicyandiamide > CN-Melamine > CN-Thiourea > CN-Urea. Notably, urea-derived g-C_3N_4 (CN-Urea) exhibited the most significantly diminished PL intensity relative to the CN-precursor photocatalysts. This markedly highlights that the CN-Urea sample had the most efficient inhibition of charge carriers recombination. Our results were consistent with the published reports by Zhang *et al.*[8] and Mao *et al.*[9] This was ascribed to the electron relocalization on surface terminal sites and more efficient photogenerated charge carrier separation in mesoporous structure of CN-Urea sample as compared to the nonporous CN-Dicyandiamide, CN-Melamine and CN-Thiourea samples.[8,9] As a result, the accelerated charge separation in the CN-Urea sample was favorable to enhance the photocatalytic performance. Owing to that, urea-derived g-C_3N_4 was chosen as the desired candidate over other precursors-derived g-C_3N_4 for the investigation in the photoreduction of CO_2 under visible light irradiation.

To further enhance the photocatalytic activity of CN-Urea, CN-Urea was engineered by rational decoration of reduction co-catalyst (graphene). Based on the unique properties of graphene and CN-Urea, the hybridization of CN-Urea with graphene in forming GCN nanostructures has become our main research focus in this study. Therefore, the construction of 2D layered heterojunction by coupling CN-Urea with graphene is anticipated to be a remarkable strategy for effective charge transfer across the graphene/g-C_3N_4 interface. More importantly, we have conducted a series of GCN samples of different precursors with similar graphene loading as demonstrated in Fig. S3B. Similar to the trend displayed by the precursors-derived pure g-C_3N_4 (Fig. S3A), the PL peak emission intensity was found to follow the order: GCN-Dicyandiamide > GCN-Melamine > GCN-Thiourea > GCN-Urea. Indeed, GCN-Urea possessed the lowest PL intensity relative to the other GCN-precursor photocatalysts. This evidently implies that the GCN-Urea sample had the most efficient inhibition of recombination of charge carriers. Based on our initial findings, we have then developed pure g-C_3N_4 and GCN hybrid nanocomposites using urea as the nitrogen-containing precursors for the detailed study in the characterizations and application in the photoreduction of CO_2 to CH_4. The subsequent sections in the ESI will all focus on the urea-derived pure g-C_3N_4 and GCN hybrid nanostructures.

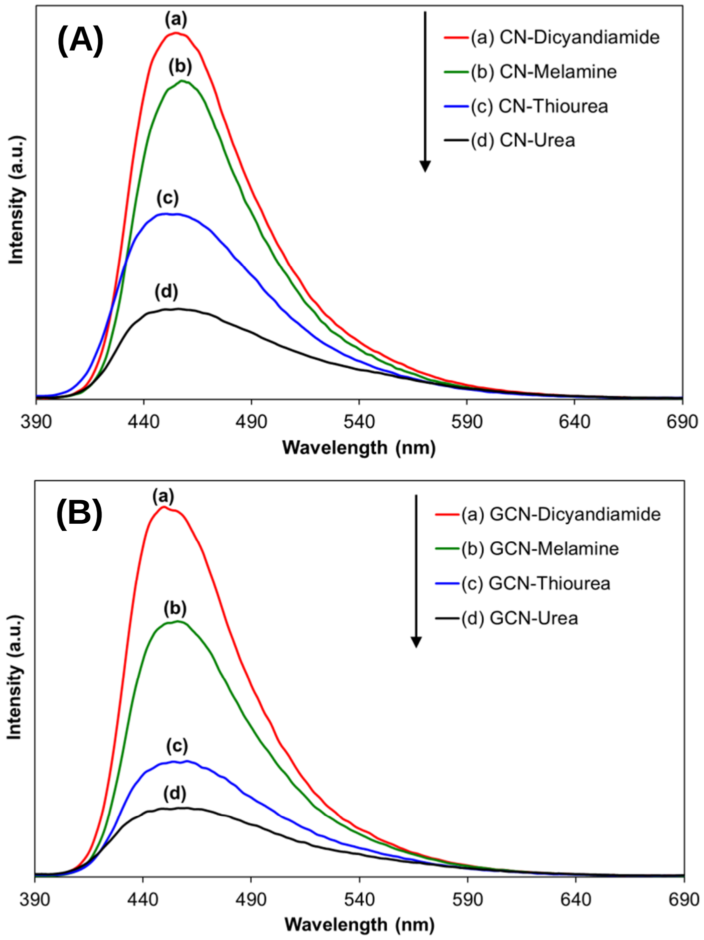

Fig. S3 PL spectra for (A) g-C_3N_4 synthesized using different precursors and (B) GCN using different precursors under 370 nm excitation.

(3) TGA plots of the as-developed photocatalysts

TGA was performed to determine the loading of graphene present in the GCN hybrid nanocomposites. Fig. S4 shows the TGA curves of GO, pure g-C_3N_4 and GCN nanocomposites. For the GO sample, it was observed that the weight loss below 300 ^{o}C was mainly caused by (1) the evaporation of adsorbed water in the interlayer spacing of the GO sheets and also (2) the decomposition of oxygen-containing functional groups such as carboxyl and carbonyl groups.[10] Compared with the curve of GO, the weight loss of GCN below 300 ^{o}C was much lower, implying that the main oxygen-containing functional groups of GO have been reduced to graphene after thermal reduction approach, which was consistent with our FTIR results. However, as observed by the TGA curve of GO, oxygen-containing functional groups in the GO were not completely removed at 520 ^{o}C, which was the temperature of the polymerization process of GCN samples in our study. In agreement with previous reports,[11-14] the decreasing trend of GO at high temperature pyrolysis after 500 ^{o}C was not an uncommon phenomenon seeing that some remaining polar functional groups on its surface were still present to act as reactive sites which were desirable to enhance its dispersibility for the fabrication of hybrid nanocomposites. Therefore, this concludes that the GCN samples contained few oxygen-containing functional groups mainly –OH groups, which was in consonance with the studies by Li *et al.*[15]

Furthermore, the decomposition of g-C_3N_4 started at *ca.* 550 ^{o}C and was completed at *ca.* 720 ^{o}C for all the GCN samples, which was higher than that of pure g-C_3N_4 at 620 ^{o}C. This was ascribed to the presence of graphene, which could act as barriers to maximize the heat insulation to protect g-C_3N_4 from the decomposition at such a high temperature. Similar findings have been observed for the case of bentonite/g-C_3N_4 composite reported by Li *et al.*[16] The residual weight percentages of the GCN nanocomposites (GCN-0.05, GCN-0.10, GCN-0.15 and GCN-0.20) were found to be 5, 10, 15 and 20 wt%, respectively, which represented the contents of graphene in the GCN samples.

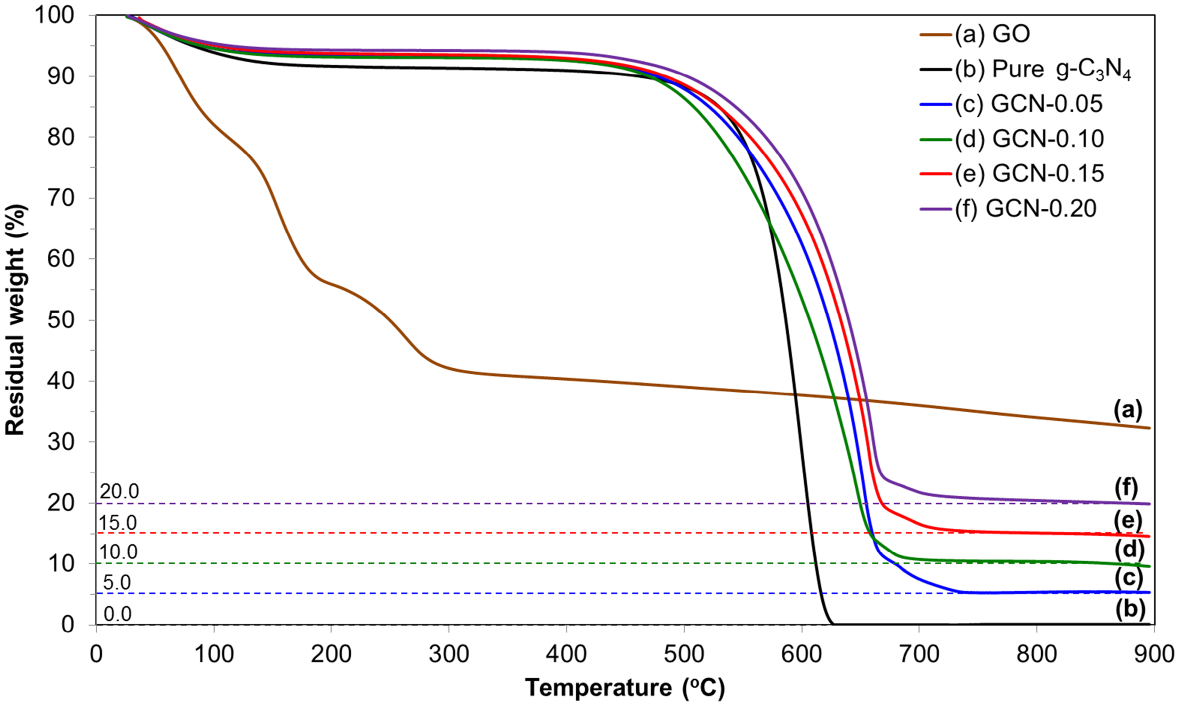

Fig. S4 TGA curves of (a) GO, (b) pure g-C_3N_4, (c) GCN-0.05, (d) GCN-0.10, (e) GCN-0.15 and (f) GCN-0.20 photocatalysts under flowing N_2.

(4) TEM image of graphene oxide and FESEM images of GCN hybrid nanostructures

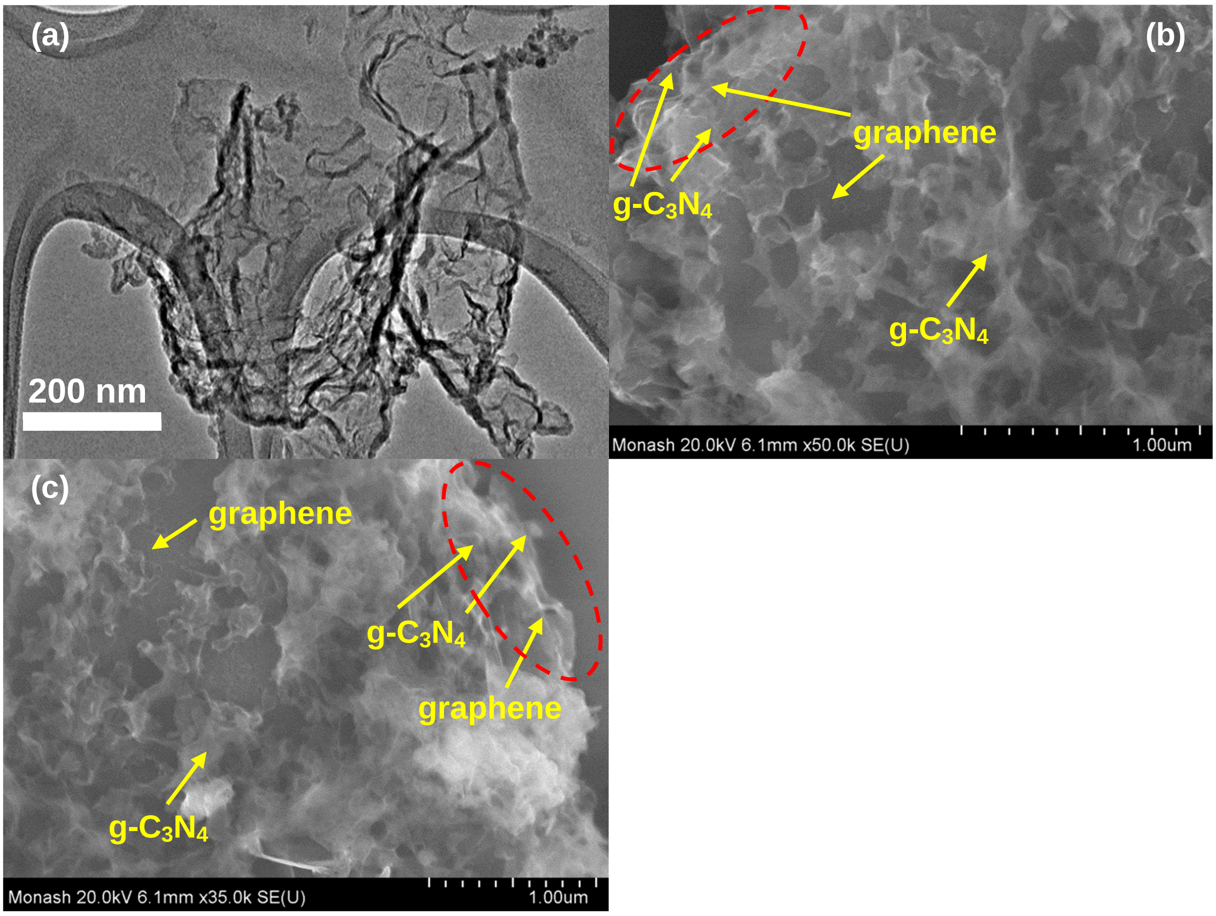

Fig. S5 (a) TEM image of graphene oxide. (b–c) FESEM images of GCN-0.15 hybrid nanocomposites at different magnifications (red dotted circles show the sandwiched section of graphene with g-C_3N_4).

(5) XRD patterns of the studied photocatalysts

The crystal structures of the GO, pure g-C_3N_4 and GCN hybrid nanocomposites with different mass ratios were characterized by XRD as shown in Fig. S6. For GO, the XRD peak at 9.5^o corresponded to the (001) interlayer spacing of 0.93 nm, which agreed well with the values reported in the literature.[17,18] Interestingly, no apparent peak of GO at $2\theta = 9.5^o$ was noted in all the GCN hybrid nanocomposites. This could be attributed to the destroy of regular stacking of GO during the thermal reduction process in forming GCN.[19] In addition, no characteristic diffraction peak of graphene ($2\theta = 24.5^o$) was observed due to the low amount and relatively low diffraction intensity of graphene.[20] The XRD patterns recorded for pure g-C_3N_4 and all GCN samples featured two distinct diffraction peaks. The weak diffraction peak at 13.0^o indexed at the (100) plane corresponds to the in-plane structural packing motif of tri-s-triazine units with an interplanar separation of 0.672 nm.[21] Another intense peak at 27.3^o represents the interlayer stacking of aromatic system with a stacking distance of 0.325 nm, ascribing to (002) diffraction planes (JCPDS 087-1526).[22-24] The basic framework of the host g-C_3N_4 remained mostly unchanged after the graphene hybridization.

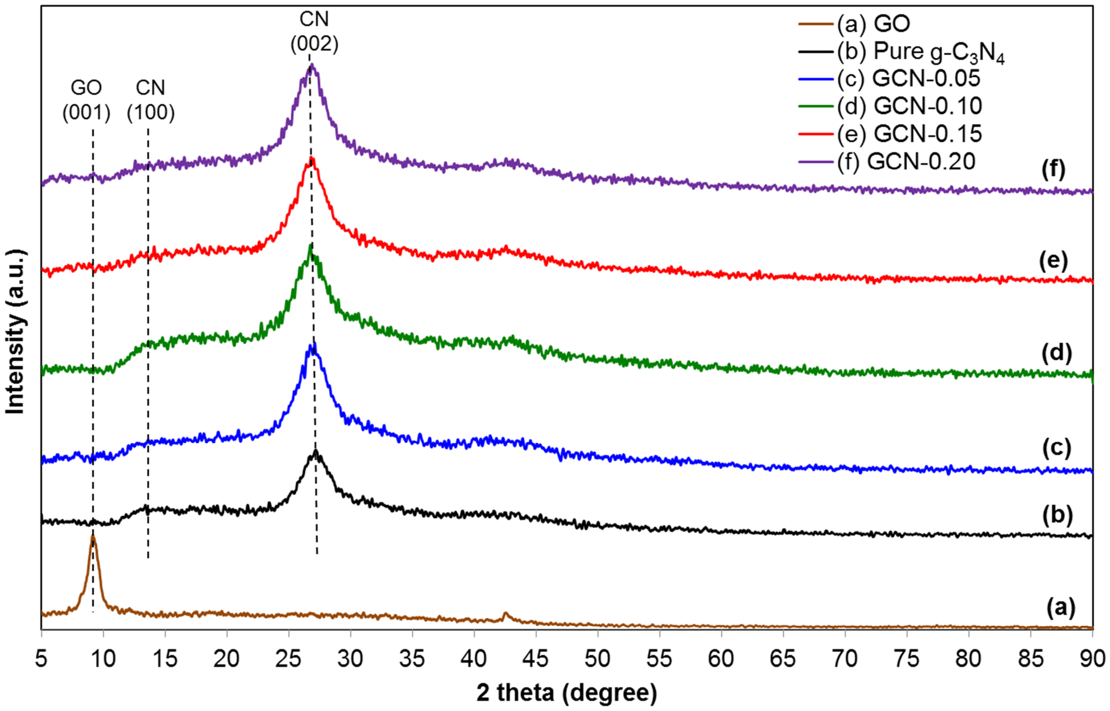

Fig. S6 XRD patterns of (a) GO, (b) pure g-C_3N_4, (c) GCN-0.05, (d) GCN-0.10, (e) GCN-0.15 and (f) GCN-0.20.

(6) EELS of the photocatalyst

Based on Fig. S7, the EELS spectrum of GCN-0.15 confirmed the existence of C and N *K* edges. The C and N atoms were sp^2-bonded within a graphitic network shown by the presence of the 1s → π^* electronic transitions for both C and N *K* edges.[25] In the C *K* edge, the peaks at 284 eV and 293 eV were ascribed to the 1s → π^* and 1s → σ^* transitions, respectively. On the other hand, the π^* and σ^* transitions in the N *K* edge located at 399 and 404 eV, respectively.[26] It is worth mentioning that the C and N *K* edges depicted similar near edge structures, implying that C and N atoms exhibited an identical threefold coordination and electronic environment in the GCN-0.15 sample.[27] The EELS result was consistent with the XRD, FTIR and XPS results shown in the manuscript.

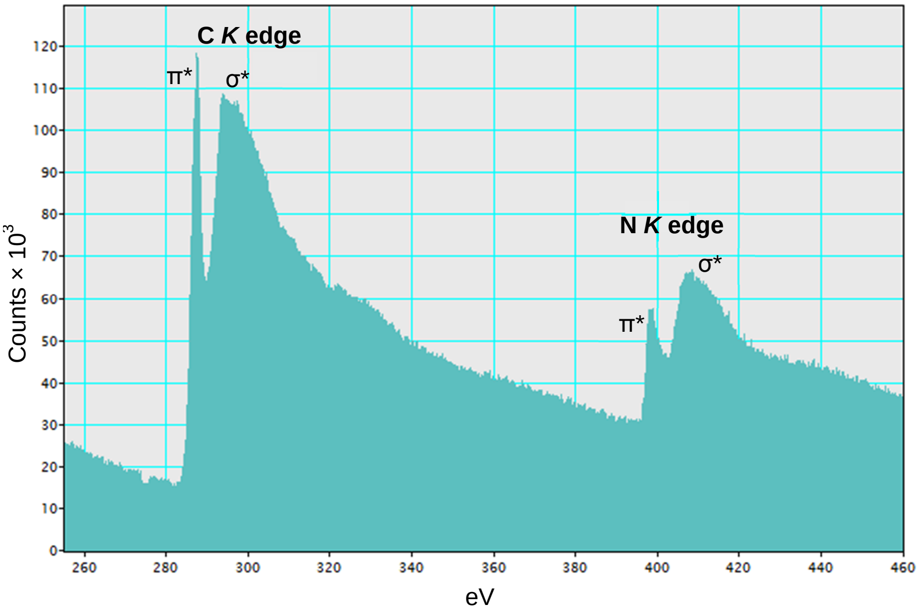

Fig. S7 EELS spectrum of C and N *K* edges recorded in the GCN-0.15 sample.

(7) UV-Vis analysis of the studied photocatalysts

The band gap energies of the photocatalysts were determined from the Kubelka-Munk (KM) function, F(R) $[F(R) = \frac{(1-R)^2}{2R}$ where R is the reflection coefficient of the sample] and the extrapolation of Tauc plot to the abscissa of photon energy.[6,28] Fig. S8 shows the plots of the transformed KM function as a function of light energy of the samples. The estimated band gap energies of pure g-C_3N_4, GCN-0.05, GCN-0.10, GCN-0.15 and GCN-0.20 were found to be 2.82, 2.80, 2.78, 2.75 and 2.70 eV, respectively. This supported the observation of a slight red shift in the absorption spectra of GCN nanocomposites (Fig. 3F in the manuscript) in comparison to the pure g-C_3N_4.

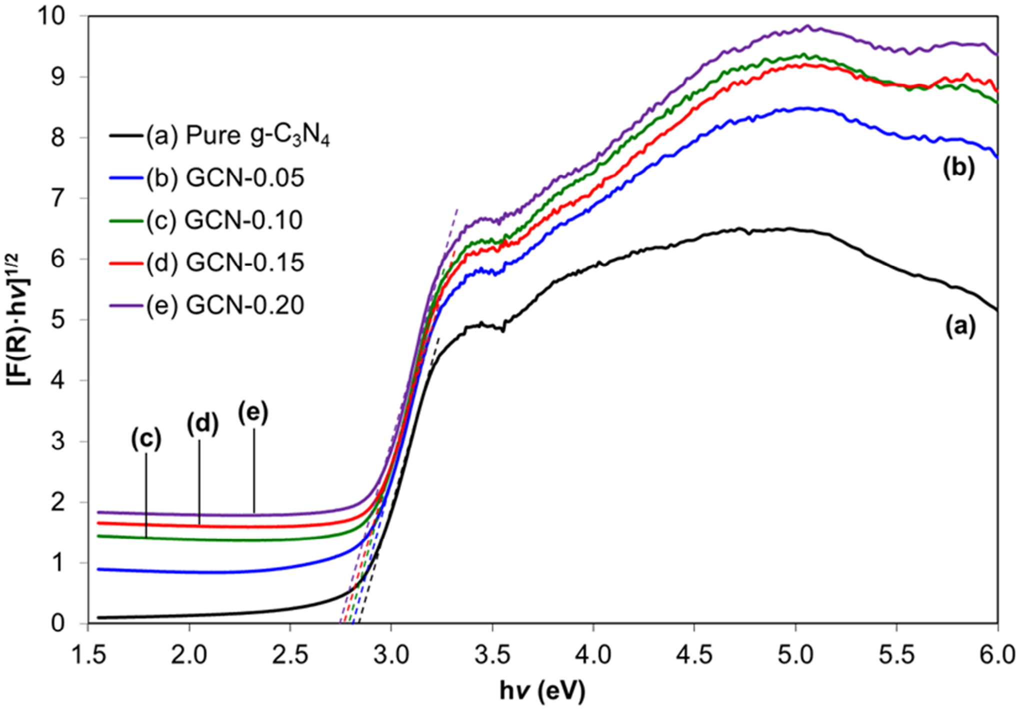

Fig. S8 Plot of transformed KM function *vs*. h*v* for (a) pure g-C_3N_4, (b) GCN-0.05, (c) GCN-0.10, (d) GCN-0.15 and (e) GCN-0.20.

(8) Control measurements of the photocatalytic reduction of CO_2

To better understand the mechanistic pathway of CH_4 formation, we have performed a series of background experiments under the following conditions: (1) without light irradiation in a flow of CO_2 and H_2O vapor, (2) under N_2 and H_2O vapor flow, (3) under CO_2 flow only without H_2O vapor, and (4) under CO_2 and H_2O vapor flow in the absence of photocatalysts. In all cases, no appreciable CH_4 gas was detected (Fig. S9). These background tests clearly confirmed that the CH_4 yield observed stemmed from the photocatalytic reduction of CO_2, and not from the photodecomposition of organic residues on the catalyst surface. This concludes that reactant feeds (CO_2 and H_2O) and visible light source are indispensable for the photocatalytic process. From our previous study,[4] GO was found to be photocatalytically active to convert CO_2 to CH_4, but the CH_4 yield was relatively low compared to GCN-0.15. When graphene alone was used as a photocatalyst, no appreciable amount of CH_4 was detected, implying that bare graphene was not active for the conversion of CO_2 to CH_4 under the experimental conditions employed.

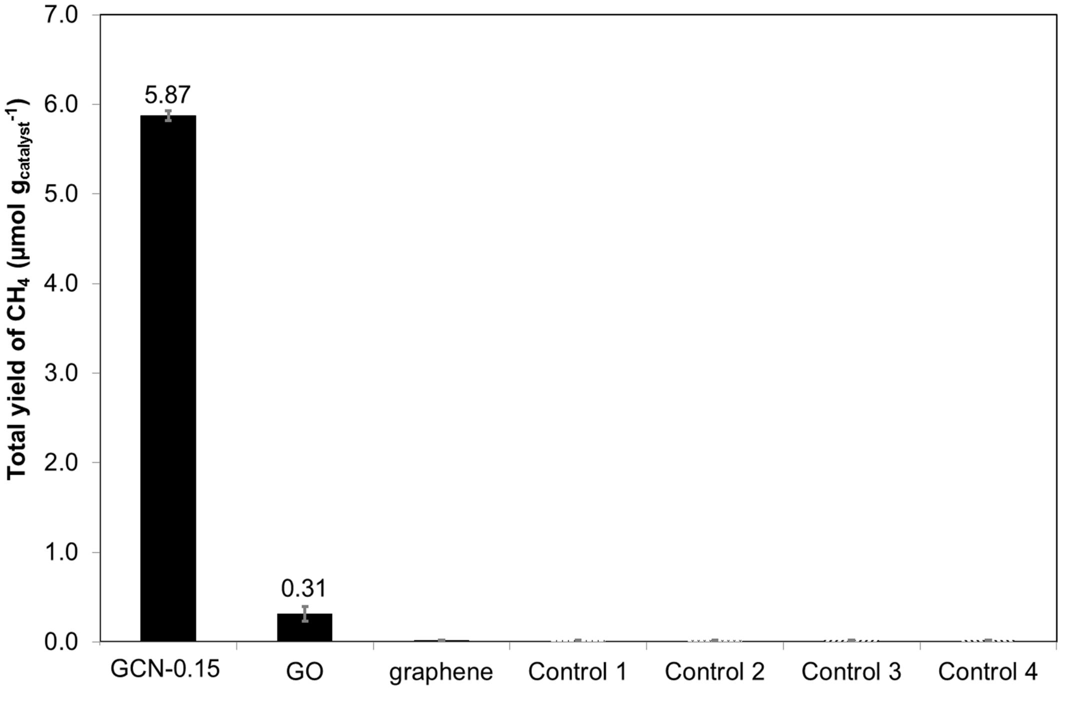

Fig. S9 Total yield of CH_4 over GCN-0.15, GO and graphene samples under visible light irradiation. Control experiments performed under four different conditions: (Control 1) without light irradiation in a flow of CO_2 and H_2O vapor, (Control 2) N_2/H_2O flow, (Control 3) CO_2 flow without H_2O vapor, and (Control 4) CO_2/H_2O flow without photocatalysts were also included.

(9) •OH trapping PL spectra of the studied photocatalysts

The formation of hydroxyl radicals (•OH) on the surface of illuminated photocatalyst could be supported by the PL technique using TA as a probe molecule. In brief, TA readily reacts with •OH to generate a highly fluorescent product of TAOH, which can be detected at a PL signal of *ca*. 425 nm.[7,29,30] Accordingly, the PL signal intensity of TAOH can be used to qualitatively identify the rate of formation of •OH, which is associated with the available hole produced on the photocatalyst.[31-33] It is well-known that •OH plays a substantial role in forming H^+ ions, which will be subsequently used to reduce CO_2 to CH_4.[3,5,34,35] Therefore, we have conducted additional experiments to estimate the ability of the photocatalysts to generate •OH under a low-power energy-saving daylight lamp. As shown in Fig. S10, GCN-0.15 displayed the highest PL intensity at *ca*. 425 nm as compared to the pure g-C_3N_4 and other GCN samples, inferring that GCN-0.15 exhibited the highest photocatalytic activity, which verified well with the photocatalytic results in Fig. 4B in the manuscript. Furthermore, it is observed that GCN-0.20 had a lower •OH trapping PL intensity than that of GCN-0.15, highlighting that the latter possessed a higher photocatalytic activity than the former owing to the greater number of •OH formed from the photocatalytic reaction. As a result, more H^+ ions were formed to reduce CO_2 to CH_4, resulting in a higher CH_4 yield in the GCN-0.15 as compared to the GCN-0.20. Overall, the results confirmed the evidence of •OH formation and participated in the photocatalytic reduction of CO_2 to CH_4.

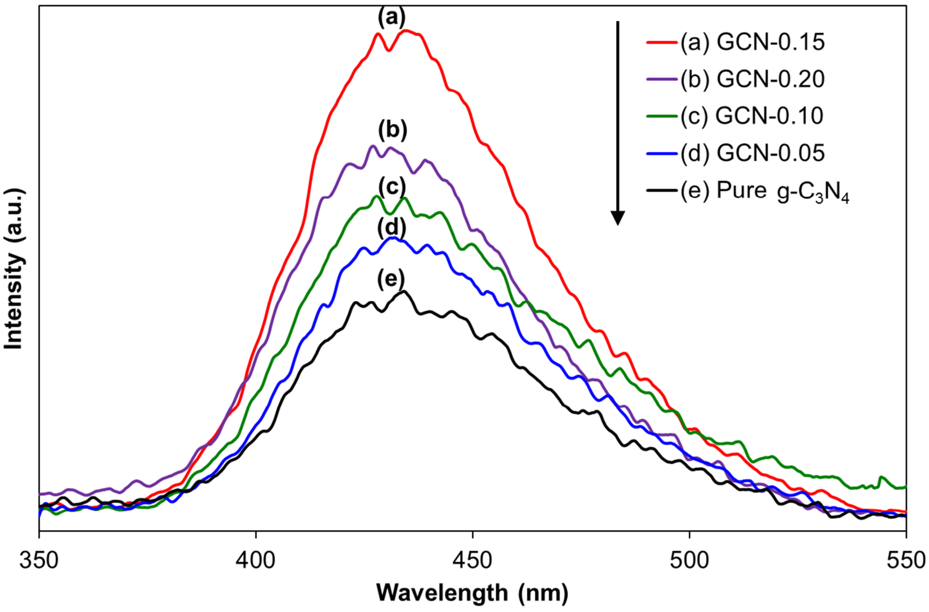

Fig. S10 •OH trapping PL spectra of pure g-C_3N_4 and GCN hybrid nanocomposites in the aqueous basic solution of TA.

(10) Possible reaction mechanism of the photocatalytic reduction of CO_2

As shown in Fig. 3F in the manuscript, g-C_3N_4 with a band gap energy of 2.82 eV could be easily excited by the visible light source of low energy content and induce the formation of electrons and holes. The valence band (VB) maximum energy level of g-C_3N_4 was measured by the VB XPS (Fig. S11a). In the present system, the VB top potential and conduction band (CB) bottom potential of g-C_3N_4 were found to be 1.40 and –1.42 eV (*vs.* NHE). These values agreed well with the reported literature.[8,36-38] It has been widely reported that the π structure of graphene facilitates the transfer of photoinduced electrons and thus could serve as excellent electron storage to prolong the lifetime of the charge carriers due to the lower Fermi level of graphene compared to g-C_3N_4.[4,39]

With the incorporation of graphene, the excited electrons from g-C_3N_4 were shuttered freely along the conducting network of graphene to inhibit the electron-hole pair recombination. The photogenerated electrons and holes initiated the photocatalytic reactions when contacted with CO_2 and H_2O (Fig. S11b). Water received the holes from the surface of g-C_3N_4 underwent photo-oxidation reaction to form H^+ protons (eqn 3). Subsequently, the H^+ protons reduced the CO_2 molecules to produce CH_4 by consuming a total of 8 electrons for each mole of CH_4 formed (eqn 4). The major reaction steps in this mechanism under visible light are summarized by eqn 2–4.

$$\text{graphene/g-}C_3N_4 \xrightarrow{hv} \text{graphene } (e^-)\text{/g-}C_3N_4\ (h^+) \qquad (2)$$

$$\text{g-}C_3N_4\ (2h^+) + H_2O \rightarrow \text{g-}C_3N_4 + 2H^+ + \tfrac{1}{2}O_2 \qquad (3)$$

$$\text{graphene } (8e^-) + CO_2 + 8H^+ \rightarrow \text{graphene} + CH_4 + 2H_2O \qquad (4)$$

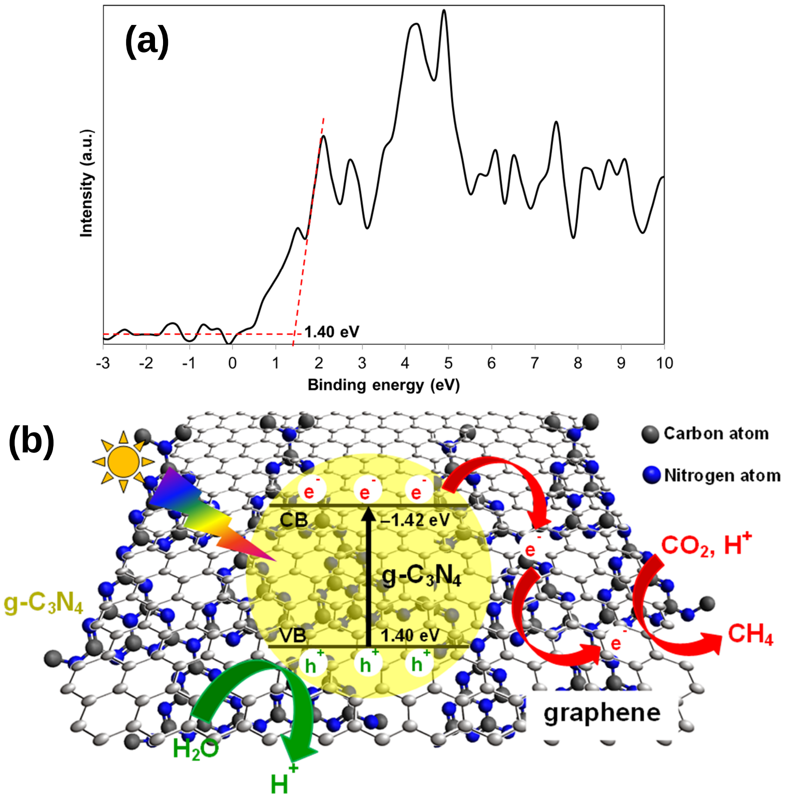

Fig. S11 (a) VB XPS curve of pure g-C_3N_4. (b) Proposed charge transfer in the GCN system for the reduction of CO_2 with H_2O to CH_4 under visible light irradiation.

(11) Enlarged figure (Fig. 3) from the manuscript

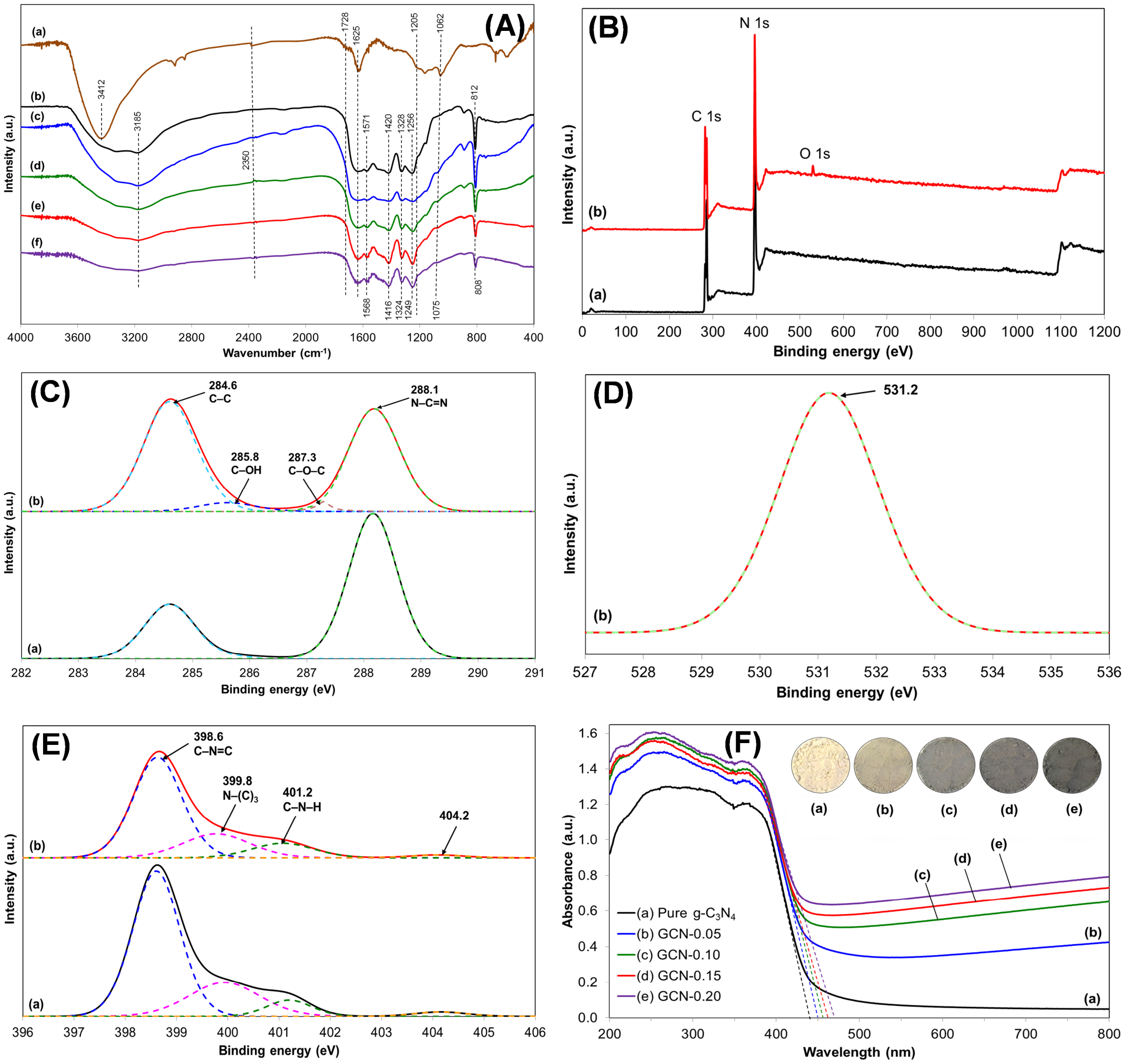

Fig. S12 (A) FTIR spectra of (a) GO, (b) pure g-C_3N_4, (c) GCN-0.05, (d) GCN-0.10, (e) GCN-0.15 and (f) GCN-0.20. (B–E) XPS spectra of (a) pure g-C_3N_4 and (b) GCN-0.15 composite: (B) XPS survey spectra, high resolution of (C) C 1s spectra, (D) O 1s spectrum and (E) N 1s spectra. (F) UV-Vis DRS (inset is the color of the photocatalysts) for pure g-C_3N_4 and GCN hybrid nanostructures.

Supplementary References

1 W. S. Hummers and R. E. Offeman, *J. Am. Chem. Soc.*, 1958, **80**, 1339-1339.

2 Y. Zhang, Z.-R. Tang, X. Fu and Y.-J. Xu, *ACS Nano*, 2011, **5**, 7426-7435.

3 W.-J. Ong, M. M. Gui, S.-P. Chai and A. R. Mohamed, *RSC Adv.*, 2013, **3**, 4505-4509.

4 L.-L. Tan, W.-J. Ong, S.-P. Chai and A. R. Mohamed, *Nanoscale Res. Lett.*, 2013, **8**, 465.

5 L.-L. Tan, W.-J. Ong, S.-P. Chai and A. R. Mohamed, *Chem. Commun.*, 2014, **50**, 6923-6926.

6 W.-J. Ong, L.-L. Tan, S.-P. Chai, S.-T. Yong and A. R. Mohamed, *Nano Res.*, 2014, **7**, 1528-1547.

7 W. Li, D. Li, W. Zhang, Y. Hu, Y. He and X. Fu, *J. Phys. Chem. C*, 2010, **114**, 2154-2159.

8 Y. Zhang, J. Liu, G. Wu and W. Chen, *Nanoscale*, 2012, **4**, 5300-5303.

9 J. Tian, Q. Liu, A. M. Asiri, K. A. Alamry and X. Sun, *ChemSusChem*, 2014, **7**, 2125-2130.

10 J.-T. Chen, Y.-J. Fu, Q.-F. An, S.-C. Lo, S.-H. Huang, W.-S. Hung, C.-C. Hu, K.-R. Lee and J.-Y. Lai, *Nanoscale*, 2013, **5**, 9081-9088.

11 J. Shen, B. Yan, M. Shi, H. Ma, N. Li and M. Ye, *J. Mater. Chem.*, 2011, **21**, 3415-3421.

12 E.-Y. Choi, T. H. Han, J. Hong, J. E. Kim, S. H. Lee, H. W. Kim and S. O. Kim, *J. Mater. Chem.*, 2010, **20**, 1907-1912.

13 S. Park, J. An, J. R. Potts, A. Velamakanni, S. Murali and R. S. Ruoff, *Carbon*, 2011, **49**, 3019-3023.

14 J. Shen, M. Shi, B. Yan, H. Ma, N. Li and M. Ye, *Nano Res.*, 2011, **4**, 795-806.

15 X. Li, H. Wang, J. T. Robinson, H. Sanchez, G. Diankov and H. Dai, *J. Am. Chem. Soc.*, 2009, **131**, 15939-15944.

16 Y. Li, J. Zhan, L. Huang, H. Xu, H. Li, R. Zhang and S. Wu, *RSC Adv.*, 2014, **4**, 11831-11839.

17 Y. Zhang, N. Zhang, Z.-R. Tang and Y.-J. Xu, *J. Phys. Chem. C*, 2014, **118**, 5299-5308.

18 S. Zhuang, X. Xu, B. Feng, J. Hu, Y. Pang, G. Zhou, L. Tong and Y. Zhou, *ACS Appl. Mater. Interfaces*, 2013, **6**, 613-621.

19 Q. Xiang, J. Yu and M. Jaroniec, *J. Phys. Chem. C*, 2011, **115**, 7355-7363.

20 Q. Li, B. Guo, J. Yu, J. Ran, B. Zhang, H. Yan and J. R. Gong, *J. Am. Chem. Soc.*, 2011, **133**, 10878-10884.

21 J. Xu, Y. Li, S. Peng, G. Lu and S. Li, *Phys. Chem. Chem. Phys.*, 2013, **15**, 7657-7665.

22 F. Dong, Z. Zhao, T. Xiong, Z. Ni, W. Zhang, Y. Sun and W.-K. Ho, *ACS Appl. Mater. Interfaces*, 2013, **5**, 11392-11401.

23 J. Tian, R. Ning, Q. Liu, A. M. Asiri, A. O. Al-Youbi and X. Sun, *ACS Appl. Mater. Interfaces*, 2014, **6**, 1011-1017.

24 Y. Min, X. F. Qi, Q. Xu and Y. Chen, *CrystEngComm*, 2014, **16**, 1287-1295.

25 T. Y. Ma, Y. Tang, S. Dai and S. Z. Qiao, *Small*, 2014, **10**, 2382-2389.

26 Y. Zhang, T. Mori, L. Niu and J. Ye, *Energy Environ. Sci.*, 2011, **4**, 4517-4521.

27 M. K. Bhunia, K. Yamauchi and K. Takanabe, *Angew. Chem. Int. Ed.*, 2014, **53**, 11001-11005.

28 S. Kumar, S. Khanchandani, M. Thirumal and A. K. Ganguli, *ACS Appl. Mater. Interfaces*, 2014, **6**, 13221-13233.

29 W.-J. Ong, J.-J. Yeong, L.-L. Tan, B. T. Goh, S. T. Yong and S.-P. Chai, *RSC Adv.*, 2014, **4**, 59676-59685.

30 W.-J. Ong, S.-Y. Voon, L.-L. Tan, B. T. Goh, S.-T. Yong and S.-P. Chai, *Ind. Eng. Chem. Res.*, 2014, **53**, 17333-17344.

31 Y.-P. Yuan, S.-W. Cao, Y.-S. Liao, L.-S. Yin and C. Xue, *Appl. Catal., B*, 2013, **140–141**, 164-168.

32 G. Liu, P. Niu, L. Yin and H.-M. Cheng, *J. Am. Chem. Soc.*, 2012, **134**, 9070-9073.

33 S. Kumar, S. T, B. Kumar, A. Baruah and V. Shanker, *J. Phys. Chem. C*, 2013, **117**, 26135-26143.

34 M. Tahir and N. S. Amin, *Appl. Catal., B*, 2015, **162**, 98-109.

35 M. M. Gui, S.-P. Chai, B.-Q. Xu and A. R. Mohamed, *RSC Adv.*, 2014, **4**, 24007-24013.

36 B. Chai, X. Liao, F. Song and H. Zhou, *Dalton Trans.*, 2014, **43**, 982-989.

37 X. Wang, K. Maeda, A. Thomas, K. Takanabe, G. Xin, J. M. Carlsson, K. Domen and M. Antonietti, *Nat. Mater.*, 2009, **8**, 76-80.

38 J. Mao, T. Peng, X. Zhang, K. Li, L. Ye and L. Zan, *Catal. Sci. Technol.*, 2013, **3**, 1253-1260.

39 W. Tu, Y. Zhou, Q. Liu, S. Yan, S. Bao, X. Wang, M. Xiao and Z. Zou, *Adv. Funct. Mater.*, 2013, **23**, 1743-1749.